PFG 2014 / 3, 0175–0188
Stuttgart, June 2014

Article

The Metrology of Directional, Spectral Reflectance Factor Measurements Based on Area Format Imaging by UAVs

Eija Honkavaara, Lauri Markelin, Teemu Hakala & Jouni Peltoniemi, Masala, Finland

Keywords: reflectance, radiometry, hyperspectral, unmanned airborne vehicle, metrology

Summary: Remote sensing based on unmanned airborne vehicles (UAVs) is a rapidly developing field of technology. New UAV sensing techniques provide attractive possibilities for measuring the reflectance properties of surfaces using vertical and oblique views. Managing the uncertainties of the reflectance measurements is crucial in many UAV remote sensing applications. We have developed a traceable procedure for conducting reflectance measurements using UAVs. It makes use of a spectrometric measurement system that is based on a UAV and a spectral imager that collects area format spectral data cubes with stereoscopic and multi-view setups. The procedure is based on reflectance panels that are positioned in the area of interest. In this investigation, we investigated the traceability of the radiometric image data processing chain. In order to take care of the uncertainty propagation, we estimated the variance-covariance propagation for the radiometric processing chain. We used the new procedure to calculate the reflectance mosaic and conduct the bidirectional reflectance factor (BRF) measurements. The estimated uncertainties were on the level of 0.01–0.04 in reflectance units.

Zusammenfassung: *Messung von gerichteten Reflektanzen bei hyperspektralen Flächenkameras auf UAVs.* Fernerkundung mit UAVs entwickelt sich derzeit schnell. Neue Aufnahmetechnologien bieten interessante Möglichkeiten zur Messung der Reflexionseigenschaften von Oberflächen. Die Beherrschung des Fehlerbudgets der Strahlungsmessungen ist für viele fernerkundliche Anwendungen entscheidend. Für den Fall der UAVs haben wir die Fehlerfortpflanzung modelliert und eine Transformationskette aufgebaut, die die Messergebnisse rückverfolgen lässt. Die Methode nutzt UAV-gestützt Hyperspektralflächenkameras für Senkrecht- und Schrägaufnahmen. Aus drei der 35 verfügbaren Kanäle wurde dann ein Orthophotomosaik der Reflektanzen erstellt und der BRF (bi-directional reflectance factor) berechnet. Als radiometrische Referenz dienten auf dem Boden ausgelegte Referenzpaneele. Zur Modellierung der Fehlerfortpflanzung schätzen wir die Varianz-Kovarianz-Matrix. Die Fehlerschätzung ergab eine Größenordnung von 0.01–0.04 der Reflektanzeinheiten.

1 Introduction

Remote sensing based on unmanned airborne vehicles (UAVs) is a rapidly developing field of technology. UAVs enable accurate, flexible, and low-cost measurements of 3D geometric, radiometric, and temporal properties of land and vegetation using cameras and other instruments. UAV sensor technology is developing rapidly and several different spectrometric imaging techniques are already available, even for light-weight systems (Hruska et al. 2012, Zarco-Tejada et al. 2012, Buettner & Roeser 2014, Saari et al. 2013).

UAVs are increasingly utilized for various environmental remote sensing applications such as for precision agriculture or water quality monitoring. They also offer an attractive alternative for producing reflectance reference measurements for a satellite sensor and image calibration and validation (cal/val) or for investigating the reflection characteristics of different surfaces and objects. For all these applications, the quality of the collected reflectance data is of great importance.

www.schweizerbart.de
DOI: 10.1127/1432-8364/2014/0218
1432-8364/14/0218 $ 3.50

Reflectance measurement by UAVs has been investigated in several recent investigations. Central challenge in the passive imaging is the impact of view and illumination geometry on the measured reflectance. This dependency is modelled by using a bidirectional reflectance distribution function (BRDF) (Schaepman-Strub et al. 2006). Hakala et al. (2010) used a micro UAV equipped with a consumer-level RGB camera to take directional reflectance measurements of snow. The results were promising; the authors concluded that the method should be further developed. Also Grenzdörffer & Niemeyer (2011) used area-format RGB images, but their approach was based a multi-camera system with vertical and oblique viewing cameras. Schwarzbach et al. (2009), Hueni et al. (2013) and Burkart et al. (2014) installed a spectrometer in a UAV to measure directional reflectance. By integrating a field spectrometer and the airborne spectrometer, these systems were able to achieve very accurate directional reflectance measurements. These investigations have proven the feasibility of the UAVs for the reflectance measurement, but also needs for further development have been identified, such as improving the spectral properties of sensors used or improving the level of automation.

SI traceability is the core concept of metrology, which is the science of measurement; it embraces both experimental and theoretical determinations at any level of uncertainty in any field of science and technology. The Bureau International des Poids et Mesures (BIPM 2004) defines metrological traceability as the "property of a measurement result whereby the result can be related to a reference through a documented unbroken chain of calibrations, each contributing to the measurement uncertainty". The level of traceability establishes the level of comparability of the measurement: Whether the result of a measurement can be compared to the previous one, to a measurement result from a year ago, or to the result of a measurement performed anywhere else in the world. Furthermore, the rigorous quantitative analysis methods can only be used for data that have been calibrated to the physical quantities. We think that traceability is an important aspect in many UAV applications.

The objective of our investigation is to develop a SI-traceable procedure for reflectance data generation based on a spectrometric UAV imaging system. In the procedure implemented at the Finnish Geodetic Institute (FGI), the steps in the reflectance transfer process are as follows: Availability of an SI-traceable reflectance standard in a national standards laboratory > Traceable reflectance at the FGI laboratory > Traceable reflectance at the measurement site > Traceable reflectance in the UAV output data. The reflectance standard can be obtained from the Metrology Research Institute at Aalto University, which is the Finnish national standards laboratory for optical quantities. Our focus is on a new kind of a spectral imager collecting area-format images, with spatially overlapping spectral data cubes in the spectral range of 400 nm – 900 nm (Saari et al. 2013, Honkavaara et al. 2013). Furthermore, in this investigation, our specific objective is to study the uncertainty resulting during the last phase of the process, the traceable reflectance in the UAV output data, which has not been rigorously studied in previous studies. This is done by developing uncertainty propagation for the image data post-processing phase.

In the following pages, we first consider the uncertainty propagation of image-based reflectance measurements in section 2. Then, we describe the method developed at the FGI in more detail in section 3. Section 4 describes an empirical campaign and in section 5 we discuss our results. Finally, we provide some conclusions based on our findings in section 6.

2 Uncertainty Propagation of Image-Based Reflectance Measurements

2.1 *Reflectance Measurement Based on Area-Format UAV Images*

The FGI system derives bidirectional reflectance factors (BRFs) using area-format images. BRF is defined as the ratio of the radiation reflected by a target of size dA ($L_s(\theta_i,\varphi_i,\theta_r,\varphi_r)$) to the radiation reflected by an ideal white isotropic (Lambertian) reflector of the same

size with similar illumination conditions ($L_{id}(\theta_i,\varphi_i)$):

$$R_s(\theta_i,\varphi_i,\theta_r,\varphi_r) = L_s(\theta_i,\varphi_i,\theta_r,\varphi_r)/ L_{id}(\theta_i,\varphi_i). \quad (1)$$

θ_i and θ_r are illumination and reflected light (observation) zenith angles, while φ_i and φ_r are the incident and reflected light azimuth angles, as shown in Fig. 1 (Schaepman-Strub et al. 2006, Suomalainen et al. 2009).

For low-altitude imagery, the central radiation components entering the sensor ($L_{at\_sensor}(\lambda)$) include the sunlight ($L_{su}(\lambda)$) and diffuse radiance ($L_{sd}(\lambda)$) reflected by the surface (adopted from Schowengerdt 2007):

$$\begin{aligned} L_{at\_sensor}(\lambda) &= L_{su}(\lambda) + L_{sd}(\lambda) \\ &= \rho(\lambda,\theta_i,\varphi_i,\theta_r,\varphi_r)\, \tau_v(\lambda)\, \tau_s(\lambda)\, E_0(\lambda) \\ &\quad \cos(\theta(x,y))/\pi \\ &\quad + F(x,y)\, \rho(\lambda, 2\pi, \theta_r, \varphi_r)\, \tau_v(\lambda) \\ &\quad E_d(\lambda)/\pi, \end{aligned} \quad (2)$$

where $\rho(\lambda, \theta_i, \varphi_i, \theta_r, \varphi_r)$ is the bidirectional spectral reflectance distribution function (BRDF) and $\rho(\lambda,2\pi,\theta_r,\varphi_r)$ is the reflectance distribution function for diffuse light, while $\tau_v(\lambda)$ and $\tau_s(\lambda)$ are the atmospheric transmittance in the view and solar paths, respectively, $E_0(\lambda)$ is the spectral irradiance on top of the atmosphere, $E_d(\lambda)$ is the spectral irradiance at the surface due to diffuse illumination, and θ is the solar incidence angle on a surface. θ_i and θ_r are the illumination and reflected light zenith angles and φ_i and φ_r are the azimuth angles, respectively. F(x,y) is the fraction of hemisphere visible to the sensor. The UAV system measures the BRF, which is directly linked to BRDF and can thus be solved based on (2).

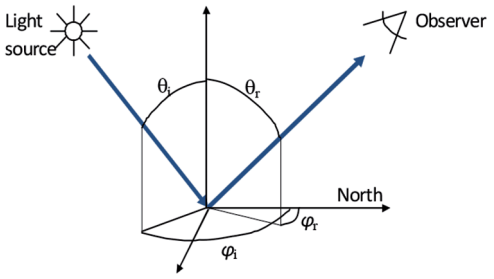

Fig. 1: Bidirectional reflectance geometry. θ_i, φ_i and θ_r, φ_r are zenith and azimuth angles of incident and reflected light, respectively.

The object is observed from different directions in the area-format images. Because of this, the images provide directional reflectance data and the field of view (FOV) of the camera determines the range of the observation angles. Two fundamentally different measurement setups that provide object reflectance are vertical block imaging and oblique BRF block imaging:

- The vertical block is collected with the camera's optical axis pointing down. The FOV of the camera determines the observation angles to the object.
- In the case of the oblique BRF block, the camera's optical axis is tilted from the vertical direction. The UAV is used to collect images around the object to provide a wide range of observation angles. The camera tilt and image FOV determine the possible observation angles.

A characteristic feature in area-format UAV imaging is that a large number of images are needed to cover the desired object area; in other words, thousands of small images are needed to provide an image mosaic for the area of 1 km x 1 km. Dozens of observations from different directions are taken for each object point.

In order to calculate the quantities of the view/illumination geometry, the solar elevation, the 3D model of the object's surface and the orientations of the images are needed. The exact view angles to the object are obtained by using the ground coordinates of the object and the position of the perspective centre. To solve the BRF, information about diffuse light and other atmospheric influences are needed. The image processing chain includes image corrections based on laboratory calibration, a determination of the orientations, digital surface model (DSM) generation, a determination of the atmospheric parameters (and radiometric model parameters), and finally, the reflectance data generation.

2.2 *Uncertainty Propagation*

In this investigation, we are assuming that the geometric quantities can be solved with a suf-

ficient degree of accuracy, and then the major remaining uncertainty components in the BRF measurement include the noise of the CCD or CMOS image, σ_{DN}, and the uncertainty of the reflectance transformation.

The reflectance transformation maps the image's digital numbers (DNs) onto the BRFs ($R(\theta_i,\varphi_i,\theta_r,\varphi_r)$):

$$R(\theta_i,\varphi_i,\theta_r,\varphi_r) = f(x), \quad (3)$$

where f(x) is the function that carries out the reflectance transformation; the *x* includes DNs and other parameters related to the reflectance transformation.

By assuming that x stands for random variables, the uncertainty of an output reflectance (σ_R) can be determined by using variance-covariance propagation techniques (Mikhail 1976):

$$\sigma_R^2 = J_f \Sigma_f J_f^T, \quad (4)$$

where J_f is the Jacobian matrix of f(x) and Σ_f is the variance-covariance matrix of the variables in the model. If we assume a simplified model where there is no correlation between the variables, the estimated standard deviation of the output reflectance value σ_R based on variance-covariance propagation is thus:

$$\sigma_R = \sqrt{\left(\frac{\partial f}{\partial x_1}\right)^2 \sigma_{x_1}^2 + \ldots + \left(\frac{\partial f}{\partial x_n}\right)^2 \sigma_{x_n}^2}. \quad (5)$$

2.2.1 Image noise

The noise in a digital image can either be a constant (fixed pattern noise) or a random type of noise (Sandau 2010). The fixed pattern noise can be eliminated to a large extent based on the laboratory calibration factors, and so achieving an accurate laboratory calibration is an essential part of the data processing chain. Important corrections include corrections for detector array nonuniformities (so-called photo response nonuniformity (PRNU) correction), lens-falloff correction, and dark signal nonuniformity correction (DSNU). The image noise can be estimated based on the signal-to-noise ratio (SNR).

2.2.2 Uncertainty of the reflectance transformation

The rigorous, physical model for the reflectance transformation is given in (2), and our ultimate objective is to develop an error propagation method for this model. In this investigation, we limit our consideration to the simple case of an empirical line-based method as described in section 4.3. In typical situations, we have an overdetermination in our estimation process, and then we can use the least squares (LS) method to calculate the model parameters and their standard deviations.

2.2.3 Implementation of the uncertainty estimation

The reflectance uncertainty estimation can be efficiently implemented in the reflectance calculation process so that an uncertainty value is provided for each calculated reflectance value. When generating reflectance image mosaics, the uncertainty estimates can be stored as images that cover the same spatial area as the image mosaic.

3 Traceable Reflectance Reference for UAV Remote Sensing Campaigns

Our procedure is based on traceable reflectance reference panels that are distributed in the area of interest. This procedure requires targets with well-behaving reflectance properties (Pagnutti et al. 2002) and traceable measurements of the reflectance characteristics.

3.1 *Targets*

A set of dark and bright targets were selected based on our analysis of the BRFs of several targets that were measured in the FGI laboratory using a FIGIFIGO goniospectrometer. The following targets were selected (Fig. 2):

- Field Spectralon: a white Spectralon reference panel 25 cm by 25 cm in size, with a reflectance of 0.99 @ 540 nm (not shown in Fig. 2).

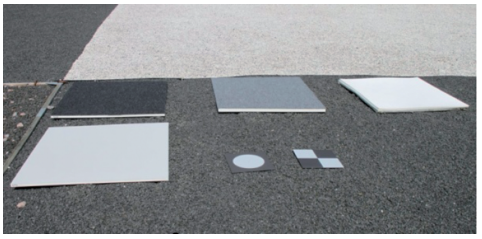

Fig. 2: Traceable reflectance panels 1m² in size. Top row: black carpet (BC) and gray carpet (GC) panels and PTFE90. Bottom row: painted grey panel (GP).

- PTFE90: a white Polytetrafluoroethylene (PTFE) panel 1 m by 1 m in size, with a reflectance of 0.90 @ 540 nm.
- 12 light grey painted panels, 1 m by 1 m in size, with a reflectance of 0.53 @ 540 nm (referred to as GP1 to GP12).
- 2 dark grey panels made of grey carpet, 1 m by 1 m in size, with a reflectance of 0.10 @ 540 nm (GC1, GC2). The carpet has a grooved surface, which might cause some directional influences.
- 2 black panels made of black carpet, 1 m by 1 m in size, with a reflectance of 0.03 @ 540 nm (BC1, BC2). The carpet has a grooved surface.

3.2 *Laboratory Measurements of Reflectance Targets*

A measurement procedure was developed to provide traceability of the BRF measurements done at the FGI for the national standards laboratory at Aalto University's Metrology Research Institute (Nevas et al. 2004). Then traceable BRFs of all the field targets were measured at the FGI laboratory using the FIGIFIGO goniospectrometer (Suomalainen et al. 2009) as follows:

- BRF of all the panels with one illumination angle (50° from zenith);
- BRF of one grey and one black carpet panel with 0°, 45°, and 90° rotation azimuth angles of the panel relative to the illumination direction;
- BRF of one grey painted panel, one black carpet and one grey carpet with two additional illumination angles (40° and 60° from zenith).

From this dataset, and with proper model fitting and interpolation, we can acquire the laboratory BRF of the targets with any illumination zenith angle between 40° and 60°, any viewing zenith angle between -70° and +70°, and any illumination and viewing azimuths freely from a full 360°.

For the grey painted panels, the results from the laboratory measurements showed that the standard deviation of reflectance for the 12 different panels was between 0.004 and 0.006 in reflectance units.

The carpets showed some directional dependency due to their grooved surfaces. For the black carpet, the maximum standard deviation of measurements when rotating the panel 0°, 45°, and 90° (azimuth angles relative to the illumination direction) was less than 0.002; for the grey carpet the corresponding value was 0.01 or less.

We concluded that the estimated standard deviation was 0.006 for the grey painted panels and black carpet, and 0.01 for the grey carpet.

4 Empirical Study

4.1 *Test Site and Ground Truth*

The procedure was evaluated at the FGI's Sjökulla remote sensing test field, located in southern Finland (60.242064 N, 24.383585 E) (Honkavaara et al. 2008). The area is covered with permanent gravel reflectance targets, permanent spatial resolution targets, and gravel field for portable targets. There is no veg-

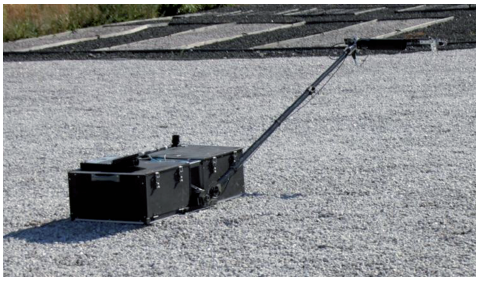

Fig. 3: The FIGIFIGO goniospectrometer measuring white gravel at the Sjökulla test field.

etation in the area (only some random weeds), and the area is practically flat.

All of the reflectance reference targets were distributed in the area. We measured the BRFs of the white, grey and black gravels and one GP panel using the FIGIFIGO goniospectrometer (Fig. 3) for reference.

A total of 85 ground control points (GCPs) with a positional uncertainty of 5 cm were available in the area; for georeferencing 19 GCPs were used. We also had a DSM with a point distance of 10 cm covering the area of interest; its estimated height uncertainty was 6 cm.

4.2 *Image Collection using UAV*

We used an eight-rotor UAV, which was based on MikroKopter autopilot and Droidworx AD-8 extended frame having a 1.5 kg payload (Fig. 4). The UAV was equipped with a stabilized camera mount, the AV130 (Photo-Higher, New Zealand), which compensates for tilts and vibrations around the roll and pitch directions.

The predominant instrument used for UAV reflectance measurements is the Fabry-Perot Interferometer-based (FPI) spectrometric camera, developed by the VTT Technology Research Center in Finland (Saari et al. 2013). This technology provides area-format spectral data cubes, but each band in the data cube has a slightly different position and orientation because they are exposed sequentially. Furthermore, the technology allows for stereoscopic and multi-ray views of objects when overlapping images are used, and an even larger range of observation angles can be obtained by using oblique views.

Fig. 4: MikroKopter UAV (top) and FPI camera (bottom).

The campaign with the FPI spectral camera took place on August 6, 2013 between 10:35 a.m. and 10:44 a.m. local time (UTC +3). The weather conditions were cloud free, providing a stable illumination level and a low level of diffuse illumination; the solar zenith angle was 53° and the solar azimuth angle was 126º.

The FPI image block consisted of two crossing, bidirectional flight lines with an oblique viewing geometry and three flight lines with a vertical viewing geometry (Fig. 5a). There were altogether 62 images. In the vertical block, the forward overlap was approximately 60% and the side overlap was approximately 50%. For the FPI camera images, the FOV was $< \pm 16°$ in the flight direction, $< \pm 27°$ in the cross-flight direction, and $< \pm 31°$ the format corner. We tilted the camera's optical axis around the axis perpendicular to the flight direction (the roll axis) using an oblique angle of 25°–30°. This provided maximum viewing angles of approximately 40° in the flight direction when the border areas of the images are not used; the rotation angles in the image block (roll, pitch, and yaw) are shown in Fig. 5b.

The flying height was approximately 40 m, which provided a ground sample distance (GSD) of 4 cm; the flight speed was approximately 4 m/s. Due to the sequential exposure of the spectral bands, the time difference between temporally adjacent bands was 75 ms, which led to a distance of 30 cm of the perspective centres. It took 1.725 s to collect a single data cube, which resulted in a spatial movement of 7.4 m (29% of the image size in the flight direction). The selected camera settings provided a total of 35 useful spectral bands in the range of 500 nm – 900 nm, with a full width of half maximum (FWHM)

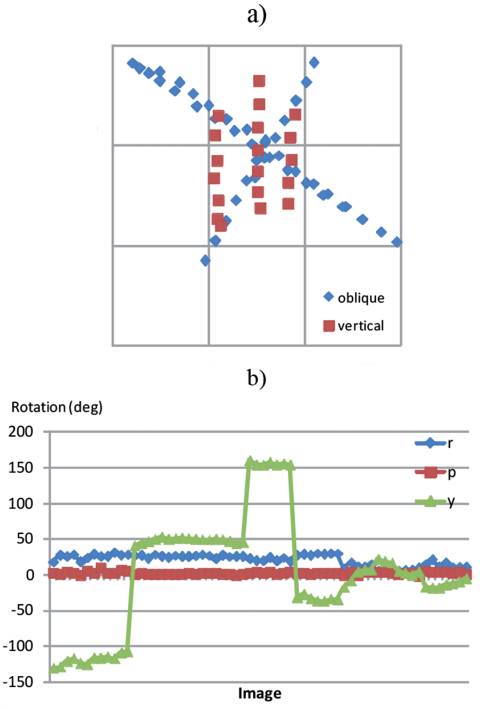

Fig. 5: a) The FPI image block with two bi-directional, oblique crossing flight lines and three vertical flight lines. b) The rotation angles roll (r), pitch (p), and yaw (y) of the images.

between 12.2 nm and 32.2 nm, on average 21.9 nm; the bands can be freely selected with one nm interval (for details, see Honkavaara et al. 2013). For further analysis, we used three bands: (central wavelength; FWHM) band 9 (534.6 nm, 30.2 nm), band 22 (634.9 nm, 16.9 nm), and band 37 (789.4 nm, 27.9 nm).

4.3 *Image Data Processing*

The image processing chain includes image corrections based on laboratory calibrations, band matching of individual bands in the spectral data cube, determination of orientations, DSM generation, atmospheric correction, and reflectance data generation. The methods used to process the FPI spectral camera data mainly consisted of generic methods for processing camera images; only the image preprocessing and band matching phases required some extra sensor-specific steps. The entire processing chain for the FPI camera was developed by Honkavaara et al. (2013).

For this investigation, a simple radiometric processing approach was used in order to better focus on our major research objective, uncertainty propagation in image processing. The model for the reflectance transformation was

$$R = (DN/a_{rel} - b_{abs})/a_{abs}. \quad (6)$$

Parameters a_{abs} and b_{abs} were estimated for one image (a reference image) located in the central area of the block using linear regression. The variable a_{rel} includes the relative parameters of each image with respect to the reference image. We carried out the processing with and without this variable. We either estimated a_{rel} by using the reflectance panels or else we used the radiometric block adjustment method presented by Honkavaara et al. (2012, 2013). Feasibility and the limitations of the model can be considered in different conditions when comparing it to the rigorous model in (1). The method requires a minimum of two reflectance reference panels.

For this model, the estimated standard deviation of the output reflectance is as follows (see (5)):

$$\sigma_R^2 = \sigma_{DN}^2/(a_{rel}a_{abs})^2 + DN^2/(a_{rel}^4 a_{abs}^2)\,\sigma_{arel}^2 + (DN^2/(a_{rel}^2 a_{abs}^4) - 2DNb_{abs}/(a_{rel}a_{abs}^4) + b_{abs}^2/a_{abs}^4)\,\sigma_{aabs}^2 + (1/a_{abs})^2\,\sigma_{babs}^2, \quad (7)$$

where σ_{arel}, σ_{aabs}, and σ_{babs} are the standard deviations of the model parameters. We implemented the uncertainty propagation method during the reflectance calculation process so that the uncertainty was estimated for each calculated reflectance value.

For the geometric processing, we used standard photogrammetric techniques (Honkavaara et al. 2013). In order to automate the processing of oblique images, we implemented the Visual Structure-from-Motion (VisualSFM) method proposed by Wu et al. (2011, 2013) for the processing line. This method was used to provide the approximate orientations for the images. The final processing was carried out using a Socet Set 5.5 photogrammetric workstation. We used 19 GCPs

for georeferencing; measuring the GCPs was the only interactive measurement step in the image processing chain.

5 Results

5.1 *Geometric processing*

Accurate georeferencing is a critical step in the process. We carried out the georeferencing for band 37 of the FPI camera. We estimated the orientations of the images and the camera parameters using a self-calibrating bundle block adjustment. The camera parameters and their standard deviations are shown in Tab. 1. After making the block adjustment, the root-mean-square error (RMSE) of residuals for the GCPs was 5.9 cm, 4.6 cm, and 7.3 cm for the FPI images at the X, Y, and Z coordinates. The good block geometry with vertical and oblique images provided good accuracy.

We interpolated the orientations of the other bands based on the trajectory of the reference band using the known time difference between the bands. These orientations are needed to provide view and illumination angles for different bands. For the reflectance orthophoto calculation, we utilized the orientations of the reference band and the bands that were rectified to the geometry of the reference band.

We calculated the viewing angles (zenith and azimuth) for all panels visible on each image based on the image and panel locations. This data, together with the solar illumination angles, was used to acquire reference BRF for each panel on each image from the laboratory FIGIFIGO measurements.

Tab. 1: Camera parameters and their standard deviations, which were obtained from the self-calibrating bundle block adjustment (x0, y0: principal point of autocollimation, f: focal length, k1: the first order radial distortion).

Parameter	Value; standard deviation
x0 (mm; mm)	-0.015; 0.0027
y0 (mm; mm)	0.012; 0.0024
f (mm; mm)	-0.073; 0.0087
k1 (mm/mm^3)	2.7E-3; 7.9E-6

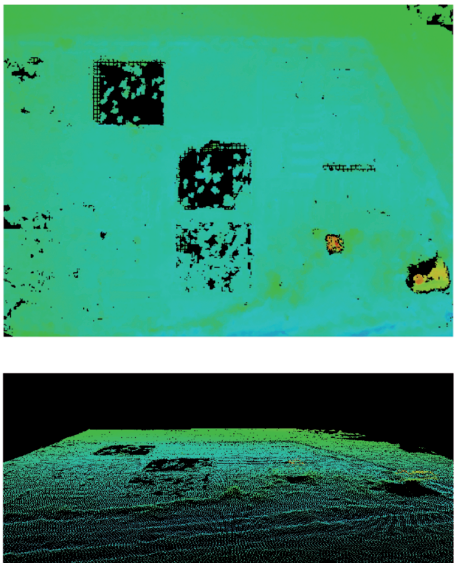

Fig. 6: DSM with a 10 cm point distance measured using automatic image matching and images from FPI camera band 37. The black areas are unsuccessful matches.

We calculated the DSM using the images from FPI band 37. Fig. 6 shows that the automatic matching was not completely successful for the black gravel targets because the SNR was too low. The 84 accurate checkpoints indicated that the RMS error in the DSM was 5 cm, which was a very good result. Because of failures at very dark targets, we used another DSM that was collected using a wide spectral bandwidth, red-green-blue (RGB) camera that provided a sufficient SNR at black targets.

5.2 *SNR*

We calculated the SNR using homogenous reflectance targets (GP1-12, GC1, GC2, BC1, BC2) as the ratio of an average signal to the standard deviation of the signal. We used a window size of 4 by 4 pixels (16 pixels) and we took a median value for all images and targets used. For the GP reflectance panel (reflectance 0.53 @ 540 nm), the SNR was better than 100 in most cases. The SNR was 50 to 100 for the darkest targets (BC) with a reflectance of 0.03 @540 nm. A decrease in the SNR appeared in the NIR bands due to the decreasing quantum

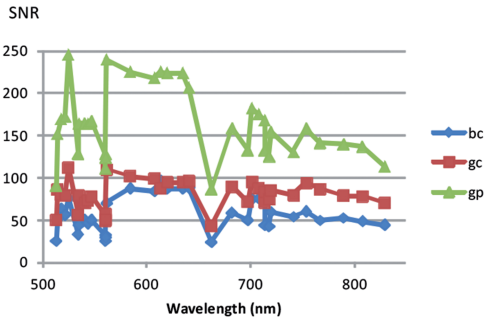

Fig. 7: SNR of the black carpet (BC), grey carpet (GC), and light grey (GP) reflectance panels as the function of the wavelength calculated in an image window 4 by 4 pixels in size.

efficiency of the CMOS image sensor with increasing wavelengths. The edge filters used in the FPI camera limited the spectral bandwidth and decreased the transmission in some of the bands, causing a decrease in the SNRs. Our objective was to ensure that the SNR is greater than 100, which means that the required noise level should be less than 1%; the results were consistent with our expectations. In the following analysis, we used an estimate of $\sigma_{DN} = 0.007$ for the image noise in the reflectance uncertainty propagation.

5.3 *Radiometric Correction*

The first results showed unexpectedly poor accuracy for the radiometric transformation. The analysis indicated that there were systematic radiometric errors in the images. It was not possible to calibrate the camera in laboratory at that point in time, so we estimated a linear correction factor with respect to the darkest corner of the image using an average image for all 62 images. Since the camera observed the object from different directions, the remaining systematic radiometric differences were most likely due to the systematic image errors. This was not a rigorous method, but we decided to use it because it improved the results greatly.

We calculated the empirical line model for one of the images located at the centre of the block with eight reflectance panels; the parameters and their standard deviations are given in Tab. 2. Then, we estimated the relative parameters (a_{rel}) for all other images (Tab. 3); there were in average 5.6 reflectance panels in image. The estimated standard deviations of the radiometric model parameters and DNs were used for the uncertainty propagation (7).

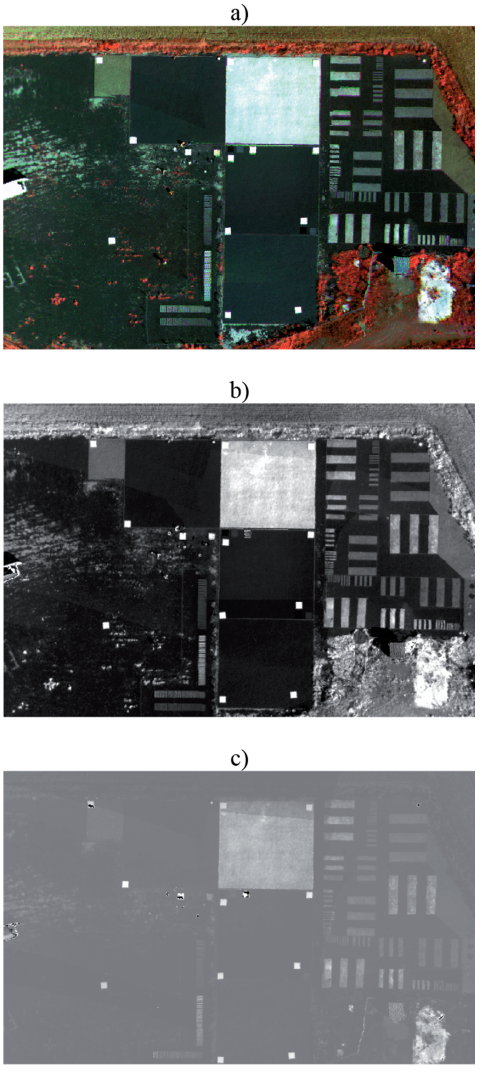

Fig. 8: a) A radiometrically adjusted composite mosaic of bands 37, 22 and 9; b) mosaic of NIR band 37; c) standard deviation plot for reflectance values in b. The maximum standard deviations were for the grey painted panels (nominal reflectance of 0.53) of 0.02–0.025, while the minimum values were for black panels (nominal reflectance 0.03) of 0.012.

Tab. 2: The empirical line parameters and their standard deviations for the reference image for each band (transformation $R = a_{abs}DN + b_{abs}$). a_{abs}, $b_{abs;}$: parameters of empirical line model; σ_{aabs} σ_{babs}: standard deviations of the model.

Band	a_{abs}; σ_{aabs}	b_{abs}; σ_{babs}
9	2.786E-05; 8.427E-07	-0.0102; 0.0120
22	2.93E-05; 9.650E-07	-0.0091; 0.0118
37	3.240E-05; 9.777E-07	-0.0353; 0.0117

Tab. 3: Statistic on the radiometric processing based on reflectance panels: RMSE of standard deviations of relative radiometric parameters (σ_{arel}), RMSE of reflectance residuals for the radiometric transformations (RMSE R), and RMSE of estimated uncertainties for different bands based on error propagation (σ_R).

Band	RMSE σ_{arel}	RMSE R	RMSE σ_R
9	0.023	0.023	0.014
22	0.030	0.028	0.013
37	0.028	0.026	0.015

We generated reflectance orthophoto mosaics using the vertical image blocks. In Fig. 8a, the mosaic is a composite of near-infra-red (NIR), red, and green bands, whereas Fig. 8b shows the mosaic of the NIR band 37. In the orthophoto mosaics, the maximum observation angles were ± 8° in the flight direction and ± 14° in the cross-flight direction. The estimated standard deviation values for Fig. 8b are given in Fig. 8c. Because we did not use the BRDF-model in the mosaic calculation, the estimated standard deviations are accurate only for the isotropic targets. The average estimated standard deviations (σ_R) were 0.013–0.015 for the different bands (Tab. 3, Fig 8c).

5.4 *BRF Extraction*

We extracted BRFs for the various targets from the UAV image block data by using DSM, orientation information, and a radio-

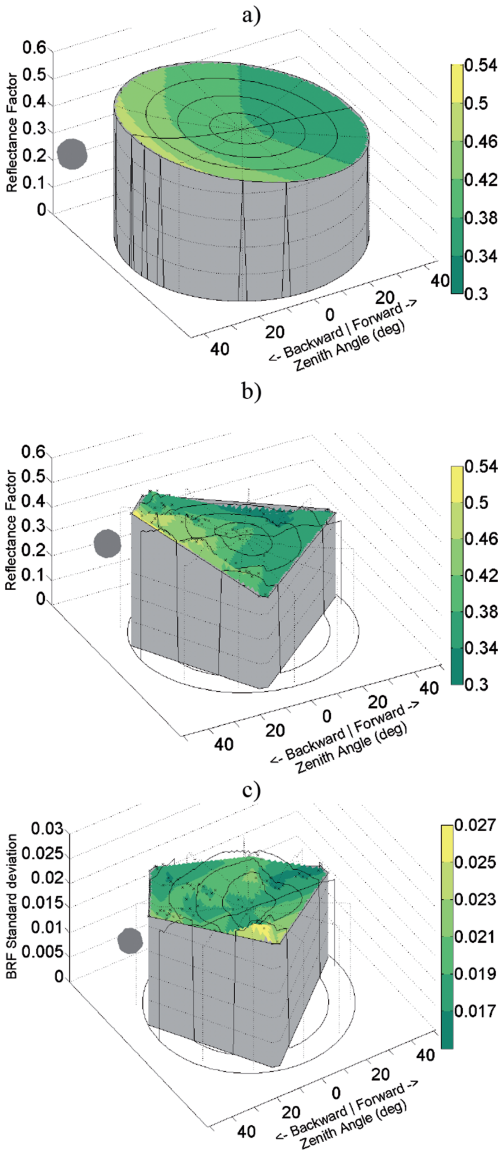

Fig. 9: BRF plot of white gravel at 790 nm measured using a) FIGIFIGO and b) UAV. c) Estimated standard deviation plot for b) based on variance covariance propagation. The illumination angle was approximately 50° above the horizon. The x-axis is the observer zenith angle at the solar principal plane; y-axis is the observer zenith angle at the plane perpendicular to the solar principal plane; z-axis is the BRF. The colour bar indicates the reflectance value (a, b) or standard deviation (c).

metric model. We used BRF observations of a single target, visible on multiple images, to create a BRF plot representing the view-angle dependency of the target. Each reflectance observation was calculated as an average in a 2 m by 2 m area. Strictly speaking, these reflectance plots include also diffuse components; when assuming that the proportion of the diffuse illumination in the clear day was 10% and the difference between the diffuse and bidirectional reflectance was 10%, the uncertainty due to this approximation was 1%, which can be considered as insignificant in this assessment.

As an example, BRF and standard deviation plots for the white gravel (nominal reflectance 0.4) are shown in Fig. 9. Some noise appeared in UAV BRF the plots (Fig. 9b). This is due to the remaining radiometric differences in the images. Nevertheless, the BRF estimates obtained when using the UAV approximated well the more accurate BRFs measured when using the FIGIFIGO (Fig. 9a). Similar conclusions could be made about the black and grey gravel. RMSEs of the estimated standard deviations based on uncertainty propagation were 0.020 for the white gravel and 0.011 for the black gravel (Fig. 9c). In the extracted data, the viewing angles were approximately 40° or less. A wider range of observation angles could be obtained by using higher oblique view angles. To provide denser BRF measurements, more flight directions could be used in the data collection in the future.

6 Discussion

UAVs offer attractive possibilities for measuring the reflectance properties of objects. We have developed a UAV system for BRF measurements that is based on a light-weight spectrometric camera collecting area-format spectral data cubes in vertical and oblique viewing directions. In this investigation, we developed an uncertainty propagation method for image processing that provides uncertainty estimates for the extracted reflectance.

Our investigation included many new aspects. 1) We used a new type of spectrometric camera to measure the spectral reflectance. Ultimately, this system is capable of measuring 3D points and their spectral characteristics. In this way, it offers an excellent possibility for controlled measurements and for rigorous characterization of the object properties. 2) Our method is based on rigorous photogrammetric techniques, which make automated and reliable procedures possible. 3) Finally, the uncertainty propagation method implemented for the processing line is a new idea in UAV remote sensing.

The image processing method has excellent automation potential. In our previous process, a bottleneck occurred when determining the approximate orientations of the images (Honkavaara et al. 2013). The implemented VisualSFM-based method (Wu et al. 2011, 2013) proved capable of automatically orienting image blocks consisting of oblique and vertical images. A further improvement will involve utilizing high-quality GPS information to support the georeferencing process.

Our reflectance transformation procedure is based on traceable reflectance panels. It is a quite laborious process; therefore, methods based on irradiance measurements on the ground and UAV should be further developed for operational applications to minimize the need for field work (Hakala et al. 2013, Burkart et al. 2014). On the other hand, the method with reflectance panels can also be considered as a portable UAV calibration test site that can be used to calibrate and validate various correction methods in different environments.

The results described in this article were preliminary and some sources of uncertainty still remain. 1) The camera calibration appeared to be inaccurate; we estimated the correction factors for the images based on the campaign image data, which caused some uncertainty in the results. 2) The diffuse light from the area surrounding the measurement site and the sky were not taken into account; this caused some inaccuracy in the BRFs. 3) The BRFs measured in the laboratory were used as a reference. In the future, we will investigate integrating the laboratory BRFs with the nadir field reflectance measurements to match the BRFs more accurate to the actual imaging conditions. This method was presented in a study by Markelin et al. (2012). 4) We assumed that the geometric measure-

ments could be considered error-free. We noticed that some discrepancies occasionally appeared, and this might have caused some minor deterioration in the level of accuracy. 5) We used a very simple approach for the reflectance transformation (6); however the developed uncertainty propagation method is a general framework and it can also be used with any reflectance transformation model. Also, further analysis of the object characteristics can be integrated with the uncertainty estimation process. 6) We used only three bands out of 35 available spectral bands. In principle, the same procedures can be repeated for other bands as well.

The measurement setup in local-area UAV applications falls between the conventional methods based on goniometric methods and airborne methods. The methodology can be further improved by adopting many of the best practices from conventional goniometric measurements (Demircan et al. 2000, Schopfer et al. 2008, Suomalainen et al. 2009) as well as from airborne measurements (Richter & Schläpfer 2002). Recently, several new ideas have been presented for UAV radiometric correction, such as downwelling and upwelling irradiance measurements in the UAV and ground (Hakala et al. 2013, Burkart et al. 2014). In the future, we will use these methods to improve our processing line.

We demonstrated the new measurement procedure in an artificial environment with gravels and reflectance panels. In our further evaluations, we will consider the method in more natural environments: in agricultural fields and in the forest.

In this investigation, the major uncertainty components in the reflectance measurement were the uncertainty of the reflectance transformation and the image quality; we assumed that the geometric processing of the measurement system was accurate and did not cause any further uncertainty. The uncertainty of the output is highly dependent upon the atmospheric conditions and camera settings (SNR). In particular, the quality of the radiometric calibration of the sensor is a fundamental factor influencing the uncertainty. With airborne hyperspectral sensors, great effort has been spent in developing accurate calibration procedures (Gege et al. 2009); with UAV camera systems, accurate radiometric calibration methods will be of importance as well (Buettner & Roeser 2014).

The overall objective for the output reflectance data quality was between 0.01 and 0.02 reflectance units; this would meet the requirements of the satellite community for global radiation budget measurements (MetEOC 2013). Our theoretical results indicated that this level of accuracy could be obtained with the proposed method. Also the empirical results were promising. However, the previously mentioned uncertainties in processing likely increased the level of uncertainty somewhat in reality. We expect that significant improvement will be made with an improved camera calibration. We will continue making the improvements for the processing method in order to improve the level of accuracy and automation, as suggested above.

7 Conclusions

We are developing SI-traceable image processing methods for UAV remote sensing. The objective is to establish the uncertainty budget of the reflectance measurements done by the FGI so that they are traceable to the reference measurements of the Metrology Research Institute at Aalto University, which serves as the Finnish national standards laboratory in optical quantities. We have implemented a method that is based on traceable reflectance panels and a traceable Spectralon. This investigation focused on the uncertainty involved in image processing. The uncertainties are propagated via image processing to provide estimates of the uncertainty of the reflectance measurements. We think that developing methods to provide reflectance data using UAV imagery and a rigorous assessment of the measurement uncertainty will be of great importance for many future UAV remote sensing applications.

Acknowledgements

We are grateful to the European Metrology Research Program (EMRP) for funding the project. The EMRP is jointly funded by the

EMRP participating countries that are part of the European Association of National Metrology Institutes and the European Union. This project is part of a Researcher Excellence Grant project, which in turn falls under the EMRP project "Metrology for Earth Observation and Climate". We acknowledge the Metrology Research Institute at Aalto University for their support in providing reflectance standard for our investigation.

References

BIPM, 2004: Web-pages of Bureau International des Poids et Mesures. – http://www.bipm.org/en/convention/wmd/2004/ (8.3.2014).

BUETTNER, A. & ROESER, H.P., 2014: Hyperspectral Remote Sensing with the UAS "Stuttgarter Adler" – System Setup, Calibration and First Results. – PFG – Photogrammetrie, Fernerkundung, Geoinformation **2014** (4), in press.

BURKART, A., COGLIATI, S., SCHICKLING, A. & RASCHER, U., 2014: A Novel UAV-Based Ultra-Light Weight Spectrometer for Field Spectroscopy. – IEEE Sensors Journal **14** (1): 62–67.

DEMIRCAN, A., SCHUSTER, R., RADKE, M., SCHÖNERMARK, M. & RÖSER, H.P., 2000: Use of a wide angle CCD line camera for BRDF measurements. – Infrared Physics & Technology **41** (1): 11–19.

GEGE, P., FRIES, J., HASCHBERGER, P., SCHÖTZ, P., SCHWARZER, H., STROBL, P., SUHR, B., ULBRICH, G. & VREELING, W.J., 2009: Calibration facility for airborne imaging spectrometers. – ISPRS Journal of Photogrammetry & Remote Sensing **64** (2009): 387–397.

GRENZDÖRFFER, G.J. & NIEMEYER, F., 2011: UAV based BRDF-measurements of agricultural surfaces with PFIFFIKUS. – International Archives of the Photogrammetry, Remote Sensing and Spatial Information Sciences **38** (1/C22).

HAKALA, T., SUOMALAINEN, J. & PELTONIEMI, J.I., 2010: Acquisition of Bidirectional Reflectance Factor Dataset Using a Micro Unmanned Aerial Vehicle and a Consumer Camera. – Remote Sensing **2** (3): 819–832.

HAKALA, T., HONKAVAARA, E., SAARI, H., MÄKYNEN, J., KAIVOSOJA, J., PESONEN, L. & PÖLÖNEN, I., 2013: Spectral imaging from UAVs under varying illumination conditions. – International Archives of the Photogrammetry, Remote Sensing and Spatial Information Sciences **40** (1/W2): 189–194.

HONKAVAARA, E., PELTONIEMI, J., AHOKAS, E., KUITTINEN, R., HYYPPÄ, J., JAAKKOLA, J., KAARTINEN, H., MARKELIN, L., NURMINEN, K. & SUOMALAINEN, J., 2008: A permanent test field for digital photogrammetric systems. – Photogrammetric Engineering & Remote Sensing **74** (1): 95–106.

HONKAVAARA, E., HAKALA, T., SAARI, H., MARKELIN, L., MÄKYNEN, J. & ROSNELL, T., 2012: A process for radiometric correction of UAV image blocks. – PFG – Photogrammetrie, Fernerkundung, Geoinformation **2012** (2): 115–127.

HONKAVAARA, E., SAARI, H., KAIVOSOJA, J., PÖLÖNEN, I., HAKALA, T., LITKEY, P., MÄKYNEN, J. & PESONEN, L., 2013: Processing and Assessment of Spectrometric, Stereoscopic Imagery Collected Using a Lightweight UAV Spectral Camera for Precision Agriculture. – Remote Sensing **5** (10): 5006–5039.

HRUSKA, R., MITCHELL, J., ANDERSON, M. & GLENN, N.F., 2012: Radiometric and geometric analysis of hyperspectral imagery acquired from an unmanned aerial vehicle. – Remote Sensing **4** (9): 2736–2752.

HUENI, A., JEHLE, M., DAMM, A., BURKART, A. & SCHAEPMAN, M., 2013: Spectroscopy Information Systems for Earth System Science. – ESA PV2013 Workshop, Frascati, Italy.

MARKELIN, L., HONKAVAARA, E., SCHLÄPFER, D., BOVET, S. & KORPELA, I., 2012: Assessment of radiometric correction methods for ADS40 imagery. – PFG – Photogrammetrie, Fernerkundung, Geoinformation **2012** (3): 251–266.

MetEOC, 2013: Web-pages of the MetEOC – European Metrology for Earth Observation and Climate. – http://www.emceoc.org/ (8.3.2014).

MIKHAIL, E., 1976: Observations and Least Squares. – IEO: 497 p., A Dun-Donnelly Publisher, New York, NY, USA.

NEVAS, S., MANOOCHERI, F. & IKONEN, E., 2004: Gonioreflectometer for measuring spectral diffuse reflectance. – Applied Optics **43** (35): 6391–6399.

PAGNUTTI, M., HOLEKAMP, K., RYAN, R., BLONSKI, S., SELLERS, R., DAVIS, B. & ZANONI, V., 2002: Measurement sets and sites commonly used for characterizations. – International Archives of Photogrammetry, Remote Sensing and Spatial Information Sciences **34** (1): 6 pages.

RICHTER, R. & SCHLÄPFER, D., 2002: Geo-atmospheric processing of airborne imaging spectrometry data. Part 2: atmospheric/topographic correction. – International Journal of Remote Sensing **23** (13): 2631–2649.

SAARI, H., PÖLÖNEN, I., SALO, H., HONKAVAARA, E., HAKALA, T., HOLMLUND, C., MÄKYNEN, J., MANNILA, R., ANTILA, T. & AKUJÄRVI, A., 2013: Miniaturized hyperspectral imager calibration and

UAV flight campaigns. – SPIE 8889, Sensors, Systems, and Next-Generation Satellites XVII.

Sandau, R., 2010: Digital airborne camera – Introduction and technology: 343 pages, Springer Science+Business Media.

Schaepman-Strub, G., Schaepman, M.E., Painter, T.H., Dangel, S. & Martonchik, J.V., 2006: Reflectance quantities in optical remote sensing – definitions and case studies. – Remote Sensing of Environment **103** (1): 27–42.

Schopfer, J., Dangel, S., Kneubühler, M. & Itten, K.I., 2008: The Improved Dual-view Field Goniometer System FIGOS. – Sensors **8** (8): 5120–5140.

Schowengerdt, R.A., 2007: Remote Sensing, Models and Methods for Image Processing. – Third edition, Academic Press Inc., San Diego, CA, USA.

Schwarzbach, M., Putze, U., Kirchgaessner, U. & v. Schoenermark, M.V., 2009: Acquisition of High Quality Remote Sensing Data Using a UAV controlled by an open source autopilot. – ASME 2009 International Design Engineering Technical Conferences & Computers and Information in Engineering Conference IDETC/CIE 2009, San Diego, CA, USA.

Suomalainen, J., Hakala, T., Peltoniemi, J. & Puttonen, E., 2009: Polarised Multiangular Reflectance Measurements Using the Finnish Geodetic Institute Field Goniospectrometer. – Sensors **9** (5): 3891–3907.

Wu, C., Agarwal, S., Curless, B. & Seitz, S.M., 2011: Multicore Bundle Adjustment. – IEEE Conference on Computer Vision and Pattern Recognition (CVPR): 3057–3064.

Wu, C., 2013: Towards Linear-time Incremental Structure from Motion. – International Conference in 3D Vision (3DV): 127–134, Seattle, WA, USA.

Zarco-Tejada, P.J., Gonzalez-Dugo, V. & Berni, J.A.J., 2012: Fluorescence, temperature and narrow-band indices acquired from a UAV platform for water stress using a micro-hyperspectral images and a thermal camera. – Remote Sensing of Environment **117:** 322–337.

Address of the Authors:

Dr. Eija Honkavaara, Teemu Hakala, Lauri Markelin & Jouni Peltoniemi, Finnish Geodetic Institute, Geodeetinrinne 2, 02430 Masala, Finland, Tel.: +358-40-192-0835 (Honkavaara), Fax: +358-9-29555200, e-mail: {eija.honkavaara}{teemu.hakala}{lauri.markelin}{jouni.peltoniemi}@fgi.fi

Manuskript eingereicht: Dezember 2013
Angenommen: März 2014